

Cassiopeia A: dust factory revealed via submillimetre polarimetry

L. Dunne,¹ S. J. Maddox,¹ R. J. Ivison,^{2,3} L. Rudnick,⁴ T. A. DeLaney,⁵ B. C. Matthews,⁶
H. L. Gomez,⁷ S. A. Eales,⁷ C. M. Crowe¹ and S. Dye⁷

¹ School of Physics & Astronomy, University of Nottingham, University Park, Nottingham NG7 2RD

² UK Astronomy Technology Centre, Royal Observatory, Blackford Hill, Edinburgh EH9 3HJ

³ Institute for Astronomy, University of Edinburgh, Blackford Hill, Edinburgh EH9 3HJ

⁴ Department of Astronomy, University of Minnesota, 116 Church Street, SE Minneapolis, MN 55455, USA

⁵ MIT Kavli Institute, 77 Massachusetts Avenue, Room NE80-6079, Cambridge, MA 02139, USA

⁶ Herzberg Institute of Astrophysics, National Research Council of Canada, 5071 West Saanich Road, Victoria, BC, V9E 2E7, Canada

⁷ Department of Physics & Astronomy, Cardiff University, Queen's Buildings, The Parade, Cardiff CF24 3AA

25 October 2021

ABSTRACT

If Type-II supernovae – the evolutionary end points of short-lived, massive stars – produce a significant quantity of dust ($>0.1 M_{\odot}$) then they can explain the rest-frame far-infrared emission seen in galaxies and quasars in the first Gyr of the Universe. Submillimetre (submm) observations of the Galactic supernova remnant, Cas A, provided the first observational evidence for the formation of significant quantities of dust in Type-II supernovae. In this paper we present new data which show that the submm emission from Cas A is polarised at a level significantly higher than that of its synchrotron emission. The orientation is consistent with that of the magnetic field in Cas A, implying that the polarised submm emission is associated with the remnant. No known mechanism would vary the synchrotron polarisation in this way and so we attribute the excess polarised submm flux to cold dust within the remnant, providing fresh evidence that cosmic dust can form rapidly. The inferred dust polarisation fraction is unprecedented ($f_{\text{pol}} \sim 30$ per cent) which, coupled with the brief timescale available for grain alignment (<300 yr), suggests that supernova dust differs from that seen in other Galactic sources (where $f_{\text{pol}} = 2 - 7$ per cent), or that a highly efficient grain alignment process must operate in the environment of a supernova remnant.

Key words: ISM – supernova remnants – supernovae: individual: Cassiopeia A – dust, extinction – submillimetre.

1 INTRODUCTION

The large quantities of dust seen in high-redshift quasars and galaxies (Priddey et al. 2003, 2008; Wang et al. 2007, 2008), at a time when the Universe was only ~ 1 Gyr old, suggests that a rapid mechanism for dust production must operate. Type-II supernovae (SNe) are good candidates for these dust factories as they evolve to a dust-producing phase in only a few hundred Myr and contain a high abundance of heavy elements. Theory predicts that each Type-II SNe should produce $\sim 0.1\text{--}1 M_{\odot}$ of dust (Todini & Ferrara 2001; Nozawa et al. 2003; Bianchi & Schneider 2007) and, if true, this can account for the dust observed at high redshift (Morgan & Edmunds 2003; Dwek et al. 2007).

Evidence for this quantity of dust forming in young SNe in the local Universe has been scant and controversial. Observations from mid-/far-infrared (IR) satellites (*IRAS*, *ISO* and *Spitzer*) detect only warm dust and find orders of magnitude less than predicted by theory (Dwek et al. 1987; Lagage et al. 1996; Douvion et al. 2001; Blair et al. 2007; Borkowski et al. 2006; Williams et al. 2006; Sugerman et al. 2006; Meikle et al. 2007), e.g. the maximum warm

dust mass inferred for Cas A from *Spitzer* data is $0.03 - 0.05 M_{\odot}$ (Rho et al. 2008). Submillimetre (submm) observations of Cas A provided the first evidence for large ($\sim 2 M_{\odot}$) quantities of colder dust manufactured in the supernova explosion (Dunne et al. 2003, hereafter D03). However, subsequent observations of CO and OH towards Cas A suggested that some or all of the submm emission may originate from dust in a foreground molecular cloud complex rather than the remnant (Krause et al. 2004; Wilson & Batrla 2005). Although the level of foreground contamination is highly uncertain – because of the difficulties in converting a molecular line intensity into a submm flux density – the molecular data have cast doubt on the idea that significant quantities of dust can form rapidly in SNe.

Another explanation for the submm excess, this time without a significant mass of dusty material, was proposed by Dwek (2004). Elongated iron needles with a much higher submm emissivity than canonical dust can also account for the far-IR and submm spectral energy distribution (SED) of Cas A. If present in the general ISM, they should contaminate the polarisation signal

from the CMB which could have importance consequences (e.g. Bowden et al. 2004).

Polarimetry at $850\ \mu\text{m}$ is extremely challenging but provides one way to test the competing hypotheses for the submm emission in Cas A: cold dust in Cas A, foreground contamination, or iron needles. We report such observations here, with the paper organised as follows: §2 describes the submm and radio polarimetry; §3 presents the results and investigates the robustness of the submm polarimetry; in §4, we use the polarimetry to place constraints on the fraction of submm emission arising from the remnant and comment on the implications for grain alignment theories.

2 OBSERVATIONS AND DATA REDUCTION

2.1 Submm observations

Our submm observations took place during 2004 October 17–18 using the SCUBA polarimeter (Murray et al. 1997; Holland et al. 1999; Greaves et al. 2003) at the 15-m James Clerk Maxwell Telescope (JCMT), Hawaii¹. We used SCUBA at $850\ \mu\text{m}$ where the array contains 37 bolometers. The instrument comprises a rotating quartz half-wave plate and a fixed photo-lithographic-grid analyser in a module that is placed in front of the SCUBA cryostat's entrance window. The weather conditions were exceptional – very stable with very little sky noise, with $\tau_{230\text{GHz}} \lesssim 0.04$ throughout. Two positions on the bright rim of Cas A were observed (Fig. 1), one in the west (hereafter W) and one in the north (hereafter N). Our original Cas A submm map (D03) was taken in SCUBA's 'scan-map' mode; for the polarimetry we were forced to make a 'jiggle' map, stepping the secondary mirror of the telescope in a 16-point pattern in order to provide a fully sampled image at $850\ \mu\text{m}$, whilst chopping a distance of 180 arcsec at around 7 Hz (the maximum possible displacement – Fig. 1 – see §3 for more discussion) to remove the atmospheric signal, and nodding the telescope every 32 s to correct for slowly varying sky gradients. A full 16-point jiggle was taken at each of 16 positions of the half-wave plate, separated by 22.5° . Thus 16 maps complete one full rotation, yielding four redundant polarisation observations. We co-added five and three such observations for the Western and Northern regions, respectively.

The submm data were reduced using the SCUBA User Reduction Facility (SURF – Jenness & Lightfoot 1998) and POLPACK (Berry & Gledhill 2001). The basic analysis consisted of removing the nod, flatfielding, correcting for extinction, flagging bad bolometers, removing sky noise and clipping noisy data. For the extinction correction, we employed a polynomial fit to the Caltech Submillimeter Observatory's 230-GHz skydip data. To remove any residual time-varying sky level, we made preliminary maps in order to choose bolometers lying in emission-free regions and then subtracted their median signal in every second of integration from the full array. We experimented with different sky bolometers and different thresholds for removing noisy bolometers to assess their impact on the polarimetry measurements. We found some small changes in the derived polarisation parameters but all maps were consistent within the errors (see §3 for more details).

Instrumental polarisation (IP) arises through the SCUBA optics and the GORE-TEX membrane in front of the dish

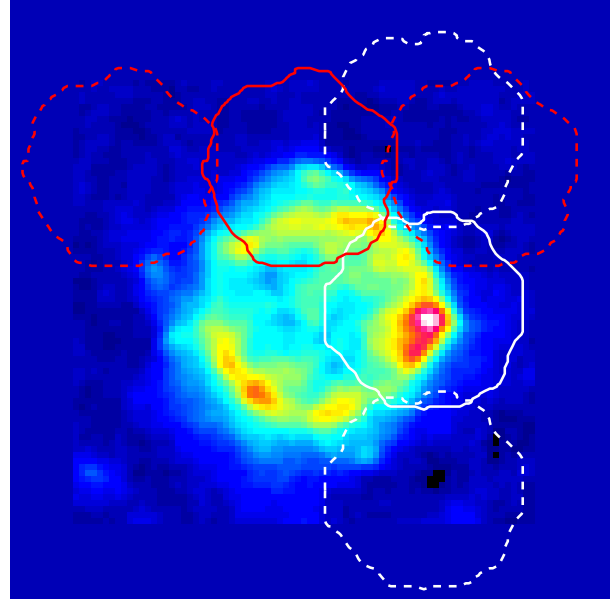


Figure 1. Cas A at $850\ \mu\text{m}$, from D03, showing the regions observed with the SCUBA polarimeter. On-source fields are denoted by solid lines while chop positions are shown by dashed lines. Position W (white) is the brightest region at radio and submm wavelengths and is coincident with a CO emission-line peak. Position N (red) is where the dust-to-synchrotron ratio is lowest and where there is no foreground emission.

(Greaves et al. 2003). IP is elevation-dependent and can be characterised by making observations of unpolarised planets. The IP was removed using the SURF task, REMIP, which uses a look-up table of bolometer IPs and corrects for the elevation at the time of the observation. The uncertainty in the IP removal is ± 0.5 per cent (Matthews et al. 2001). Once treated in this way, each integration was re-gridded separately using a Gaussian weighting function with a scale of 7 arcsec (approximately half the FWHM for SCUBA at $850\ \mu\text{m}$) onto 6.2-arcsec pixels (the step size of the jiggle pattern), ready for the polarisation analysis. From each complete polarimetry observation, four degenerate maps are made for each of the four equivalent waveplate angles. The four maps at each angle are stacked and the variance for each pixel calculated from the scatter between the four maps. POLPACK was then used to derive the Stokes U , Q and I values for each pixel in each complete polarimetry observation by fitting the following function to the data (Sparks & Axon 1999)

$$I_k' = \frac{t}{2} [I + \epsilon(Q \cos 2\phi_k + U \sin 2\phi_k)]$$

where I_k' is the expected intensity in image k , ϕ_k is the position angle of the wave plate after correction for the parallactic angle for image k , t is the analyser transmission factor and ϵ is the polarising efficiency factor. The error in each Stokes parameter is derived from the input variances.

These I , Q and U images were then median stacked for repeat observations and a final data cube was created. Polarisation fractions, p , and position angles (PAs), θ , were derived from the Stokes parameters (Hildebrand et al. 2000) after correcting for the Ricean bias – i.e. the increase in p that results from constraining p to be positive even when Q and U are consistent with $p = 0$. Ricean bias is a significant effect for low signal-to-noise measurements ($\text{SNR} \lesssim 2$).

¹ The JCMT is operated by the Joint Astronomy Centre on behalf of the Science and Technology Facilities Council of the United Kingdom, the Netherlands Organisation for Scientific Research, and the National Research Council of Canada.

We define the normalised Stokes parameters and associated errors as

$$u = U/I; \quad q = Q/I$$

$$\sigma_q = \left(\frac{\sigma_I^2 q^2 + \sigma_Q^2}{I^2} \right)^{1/2}; \quad \sigma_u = \left(\frac{\sigma_I^2 u^2 + \sigma_U^2}{I^2} \right)^{1/2}$$

Debiased p values are calculated using

$$p = \frac{\sqrt{q^2 + u^2 - \Delta}}{I} \times 100 \text{ per cent} \quad (1)$$

where the bias is given by

$$\Delta = \frac{q^2 \sigma_q^2 + u^2 \sigma_u^2}{q^2 + u^2} \quad (2)$$

The error in p is $\sigma_p = \sqrt{\Delta} \times 100$ per cent. The polarisation PA – the position of the electric field vector measured relative to Celestial North – is given by

$$\theta = 0.5 \arctan \left(\frac{U}{Q} \right) \quad (3)$$

The error on θ is given by $\sigma_\theta = \frac{\sigma_p}{p} \times 28.6^\circ$.

The polarisation data were binned to a resolution of 18 arcsec to improve the SNR. Vectors were chosen for the catalogue if $\sigma_p < 4$ per cent, thereby removing unreliable vectors in regions of high noise. We have also imposed a cut of $\text{SNR} \geq 2$ in p as vectors with below this level have large errors in θ and the bias correction we make is really only applicable at $\text{SNR} \geq 2$ (Hildebrand et al. 2000). The SNR cut affects only 2/57 vectors and has no consequences for our results (see § 3.2). The absolute accuracy in position angle is limited by the systematics of removing the sky noise. This was found to be $\pm 6^\circ$.

As discussed by Greaves et al. (2003), there is a minimum believable polarisation percentage within the main beam of SCUBA polarisation maps due to potential contamination of the polarisation signal from the extended sidelobes of the JCMT beam. The value of the minimum believable polarisation is given by the relation

$$p_{\text{crit}} \geq 2 p_{\text{sl}} P_{\text{sl}} \frac{S_{\text{sl}}}{S_{\text{mb}}} \quad (4)$$

where p_{sl} is the polarisation in the sidelobe (i.e. off-centre position) and P_{sl} is the power in the sidelobe relative to the main beam (measured from planetary observations). The flux at the position of an off-centre source relative to the flux at the map centre is given by $S_{\text{sl}}/S_{\text{mb}}$. We have used observations of Uranus, obtained at the time of the Cas A observations, to assess the value of p_{crit} and thereby measure the sidelobe polarisation for our science data.

The highest value of p_{crit} will be measured for the largest ratio of $S_{\text{sl}}/S_{\text{mb}}$. This value arises for our observations of the northern rim of Cas A, in which the brightest peak in the field of view does not lie at the array centre. For these observations, we measure a flux ratio of 1.1 relative to the centre of the array. The power in the beam within this annulus ($49.0 < \sqrt{\Delta\alpha^2 + \Delta\delta^2} < 61.8$ arcsec, where α and δ represent R.A. and Dec.) is 0.014 relative to the main beam, and the IP measured within the same annulus is 9.2 ± 4.6 per cent. The highest value of p_{crit} is therefore 0.3 ± 0.2 per cent. We can therefore accept that all values of p in excess of 0.5 per cent arise from the remnant itself. Since all measured values exceed this threshold by a significant margin, it is clear that none of the measurements are due to polarisation in the sidelobe positions.

Table 1. Summary of VLA observations.

Configuration	Date	Bandwidth	Duration
A	2000.9	6.25 MHz	12 hr
B	2001.2, 2001.3	12.5 MHz	11 hr
C	2000.3	25.0 MHz	6.0 hr
D	2000.7	25.0 MHz	4.5 hr

2.2 Radio observations

Cas A was observed with the National Radio Astronomy Observatory's (NRAO²) Very Large Array (VLA) in 2000–01 using all four configurations from the most extended (A) to the most compact (D). Data were taken at four frequencies, 4605, 4720, 4860 and 4995 MHz, as summarised in Table 1.

Standard calibration procedures were employed, as outlined in the *AIPS* cookbook³ using 3C 48 to set the flux density scale, 3C 138 to calibrate the polarisation and J2355+498 as a local phase calibrator. After initial calibration, multiple passes of self-calibration were performed to improve the antenna phase solutions.

The *AIPS* maximum entropy deconvolution routine VTESS, which maximises smoothness in an image, was used to restore the total intensity images and the corresponding routine UTESS, which maximises emptiness in an image, was used to restore the Stokes Q and U images. An 18-arcsec beam (FWHM) was used for deconvolution, to match the resolution of the submm data. The standard primary beam attenuation correction was applied in the VTESS and UTESS routines. The total restored flux density was 788 Jy. Noise-corrected, linearly polarised intensity, polarisation percentage, and polarisation PA images were made from the Stokes I , Q and U maps. The total polarised flux density was 28.9 Jy, resulting in an average polarisation percentage of 3.7 per cent.

To enable a comparison with the submm data, the radio IQU datacube was aligned with the submm pixels using the Kernel Application Package (KAPPA) task WCSALIGN. Polarisation vectors were then calculated in the same way as for the submm data, but using bespoke MATLAB scripts. Radio vectors with $\sigma_p < 2.4$ were chosen, providing complete coverage of the regions where we have submm vector information.

3 RESULTS

The SCUBA 850- μm polarimetry vectors are shown in Fig. 2, alongside the 5-GHz radio vectors. The underlying images are the 850- μm scan-map from D03 and the 5-GHz image, both convolved to the same resolution as the binned polarimetry data. The length of the vectors represents the degree of polarisation, p , and their PA shows the direction of the magnetic (B) field (i.e. the E vectors measured from the Stokes parameters have been rotated by 90° for display purposes).

These images clearly show that the submm emission is significantly more polarised than the radio emission, with vectors that trace the approximately radial magnetic field in the remnant. Both traits indicate a source of polarised emission in Cas A above a general extrapolation of the synchrotron polarised flux density.

We will now investigate in more detail the robustness of this

² NRAO is a facility of the National Science Foundation operated under cooperative agreement by Associated Universities, Inc.

³ www.aips.nrao.edu/cook.html

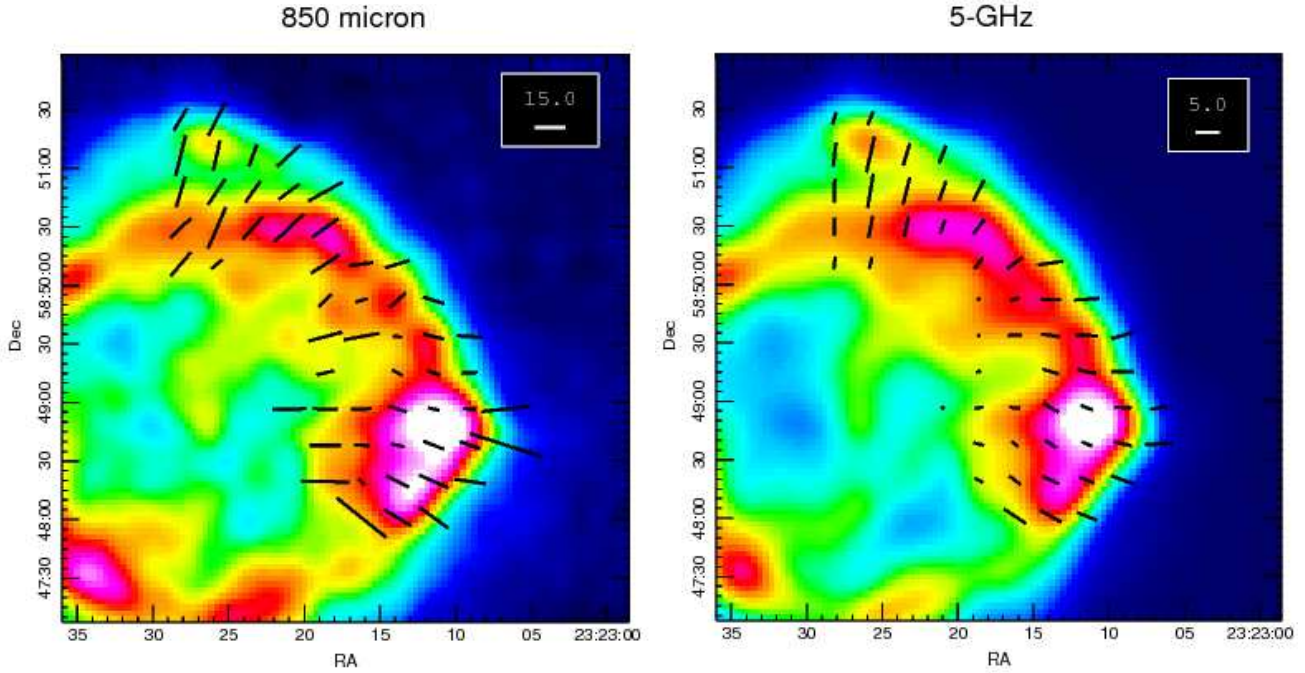


Figure 2. *Left:* 850- μm polarimetry vectors overlaid on the 850- μm map from D03. *Right:* 5-GHz polarimetry vectors overlaid on the 5-GHz map. All maps are at the same resolution, 18 arcsec. Vectors are rotated by 90° to show the direction of the magnetic field. The orientation of the submm vectors clearly trace the approximately radial B field of the remnant. The 5-GHz vectors have been corrected for an average rotation measure of -110 rad m^{-2} .

result and explore whether the submm polarisation is due to dust or synchrotron emission.

3.1 Robustness of results

In this section we will describe our investigation into the robustness of the data through comparing several reductions of the polarimetry data and also through a simulation of the effects of chopping. We conclude that the data are robust and that chopping cannot conspire to affect our conclusions. Readers who wish to skip the technical details can move on to § 3.2.

3.1.1 Data-reduction issues

We explored the effect of using different sky bolometers and clipping thresholds whilst reducing the submm data (§2). The choice of sky bolometers is important as several effects can cause a bolometer's signal to vary with time during a polarimetry observation:

- (i) A changing sky level, which should correlate across all bolometers.
- (ii) Bolometers jiggling on and off a bright source. This is the rationale behind choosing off-source bolometers to remove sky variations across the whole array.
- (iii) Bolometers may lie on regions of the same brightness throughout an observation but see polarised emission which changes as a function of wave-plate angle, and therefore as a function of time within the observation.

If bolometers displaying effects (ii) or (iii) are used to remove sky noise, they could introduce a temporal signal variation to the rest of the array and cause systematic changes in the derived polarisation properties.

We tried two sky-removal techniques: the first used as many bolometers as possible, whilst avoiding bright emission regions; a second, more conservative approach used only bolometers two rows away from bright emission. We found small changes in p ($\Delta p = -0.3$) and θ ($\Delta \theta = -7^\circ$) but the differences between the reductions are consistent with the errors derived from the distributions in each map ($\sigma_p = 1.2$, $\sigma_\theta = 4^\circ$). As the first method uses bolometers which may have jiggled onto polarised emission, we will use the second, more conservative approach for the rest of the analysis. Our overall conclusions are unaffected by this choice of sky-removal technique.

We have also compared our maps to the data presented by Matthews et al. (2008) where the mean sky level was not removed from the array (only the variations are removed) and bolometers showing excess noise were flagged aggressively, resulting in the removal of around 30 per cent of the data. We have taken a slightly different approach, flagging only the four bolometers with clear excess noise, plus one that was dead: around 13 per cent of the data in total. The time series of many bolometers removed by Matthews et al. (2008) displayed momentary spikes but were otherwise in line with the rest of the array. We de-spiked these by flagging any data more than 3σ from the mean. Overall, the mean p and θ derived from both reductions are consistent within the errors ($\Delta p = 1.0$ and $\Delta \theta = -5^\circ$). We conclude that the data are robust to minor changes in the data reduction procedure.

3.1.2 Chopping

We investigated the effects of chopping onto either polarised or unpolarised emission, something which can potentially have a serious impact on submm polarimetry data (Hildebrand et al. 2000). We synthesised Q and U for our reference positions using either the radio values scaled to 850 μm or assuming a value for p and θ for the

interstellar medium (ISM) surrounding Cas A (these are described in more detail below). The Q and U values from our submm polarimetry data were then corrected by adding half of the Q and U values found at each reference position. The I values were taken from the 850- μm scan-maps, which comprised the D03 flattened and unflattened reductions (hereafter A and B), the former with large-scale undulations removed, and the map used by Krause et al. (2004) (hereafter C). We created a simulated ‘chopped’ image from our measured Q and U values, and a ‘chopped’ I image from the scan map after processing it with the chopping simulator. This is intended to represent the data we measure. We then correct for the chopping in Q , U and I and produce a ‘corrected’ map. This assumes, of course, that the scan-maps provide a good representation of unchopped data (they are the best we have). Chopping onto unpolarised flux should not affect θ but will influence p . We have thereby simulated the range of plausible structures around Cas A to probe the possible systematics. In utilising the unflattened scan-maps we have assumed that any structure is real and not an artefact of the data reduction.

In the first instance we assumed that only flux associated with the remnant was polarised and used the radio Q and U maps to estimate the flux of polarised synchrotron in the reference beams. We accounted for a rotation of 24° in going from 5-GHz to 850- μm , in line with the rotation measures derived by Jones et al. (2003) and Anderson et al. (1995). We scaled the radio Q and U values to 850- μm using the value of the synchrotron spectral index at the reference points ($\alpha \sim -0.74$) and increased the polarised flux in the reference positions by a factor three, roughly the average ratio of $p_{\text{submm}}/p_{\text{radio}}$ that we observe, to allow for the reference beams being polarised at the same level as the central field. The results are summarised in Table 2. We found that chopping onto remnant emission polarised at the level seen in the submm would have a small effect on the submm vectors, with an average increase in p of $+0.6$ per cent and an average rotation of $+0.4^\circ$.

We next investigated the possibility that any foreground submm emission in the reference positions is polarised. We allow all of the submm emission in the reference positions to be polarised at the level found in clouds in the vicinity of Cas A by the *Archeops* submm balloon experiment (Benoît et al. 2004), which is 23 per cent at $\theta = -\pi/3$ and 12 per cent at $\theta = \pi/8$. It is not certain that the Cas A foreground emission is polarised at this high level as the clouds in Benoît et al. are $> 2^\circ$ away, but we consider this as the most conservative case. We find that the difference in the chopped and unchopped maps is $\Delta p = 0.3 - 1.2$ in field W and $\Delta p = 0.2 - 1.9$ in field N. The rotation introduced by chopping is small, the largest being $+1.2^\circ$ in W and -2.7° in N. These simulations are shown in Fig. 3 and the results summarised in Table 2. None of the small changes introduced by chopping alter our conclusions.

3.2 Submm and radio polarisation properties

Polarisation vectors were created as described in § 2.1 using the same positions in the observed 850- μm and 5-GHz images. We also predict the observed polarisation expected at 850 μm , given the measurements in hand at 5 GHz and assuming that the excess submm emission is unpolarised. We scale the 5-GHz Q and U fluxes using a 1.4 GHz/5 GHz spectral index map. We use the submm scan-map from D03 as the I image, since this exceeds the predicted synchrotron flux by ~ 30 per cent (due to dust emission, either in the supernova remnant or in front of it). We then calculate p using the scaled radio Q and U data and the submm I data.

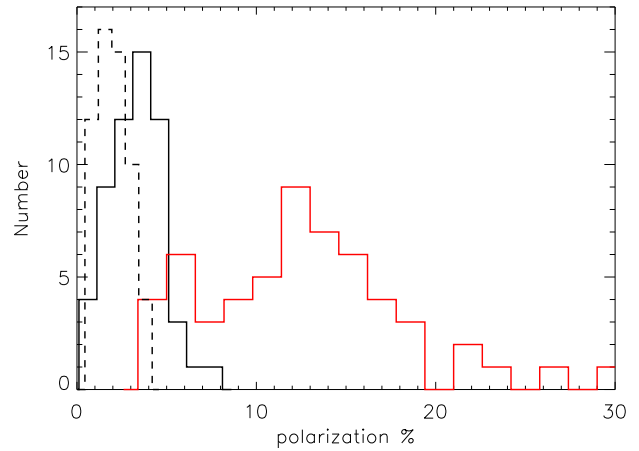


Figure 4. Histogram showing the distribution of p for the 5-GHz data (black) and the 850- μm data (red). The distributions are significantly different. The predicted polarisation at 850 μm , using the 5-GHz data as described in the text, is shown by the dashed line.

This is the polarisation we would expect if the submm I emission consisted of synchrotron and unpolarised dust.

A comparison of the p distributions in the radio and submm wavebands is shown in Fig. 4 where it is clear that the submm emission shows a significantly higher degree of polarisation than does the radio. The means of the distributions are $p_{\text{submm}} = 13.5 \pm 0.8$ per cent and $p_{\text{radio}} = 3.7 \pm 0.2$ per cent when selecting vectors at $p/dp \geq 2$ and $dp < 4$ per cent in the submm waveband. If the SNR threshold is ignored, the mean p_{submm} drops slightly to 12.9 ± 0.9 per cent. The means are thus different at the $> 8\sigma$ level. If we compare to the predicted values at 850 μm (dashed histogram in Fig. 4) the difference becomes even more pronounced. The results of the chopping simulations suggest a minor reduction in p_{submm} of order 0.7 per cent may be required, but there appears to be no possibility of reconciling the two distributions.

Having established a clear excess in polarisation at 850 μm , we now wish to understand whether this difference is due to a reduction in the level of synchrotron polarisation between 850 μm and 5 GHz via a depolarising mechanism in the remnant, or to an extra source of polarised emission at 850 μm (i.e. aligned dust grains).

Synchrotron emission in supernova remnants should be highly polarised (~ 70 per cent) but observed polarisations at radio frequencies in young remnants like Cas A are typically much lower, implying that the magnetic field is highly disordered on scales below an arcsec (Milne 1987). Another cause of reduced polarisation at radio wavelengths is rotation due to the Faraday effect, in which the plane of polarisation is rotated as the polarised waves pass through a magnetised plasma. This effect is wavelength-dependent, with longer wavelengths suffering more rotation. Emission from regions at different depths in the plasma of Cas A will be rotated by differing amounts as they travel to the observer. This causes ‘internal depolarisation’ at the wavelengths which undergo the most rotation.

Depolarisation at radio frequencies has been studied in Cas A and found to be negligible at frequencies of $\gtrsim 5$ GHz. From 5 GHz to 2.2 μm , the fractional synchrotron polarisation remains roughly constant (4–7 per cent, Jones et al. 2003; Anderson et al. 1995; Kenney & Dent 1985) which suggests that the much higher polarisations observed at 850 μm cannot be due to synchrotron radia-

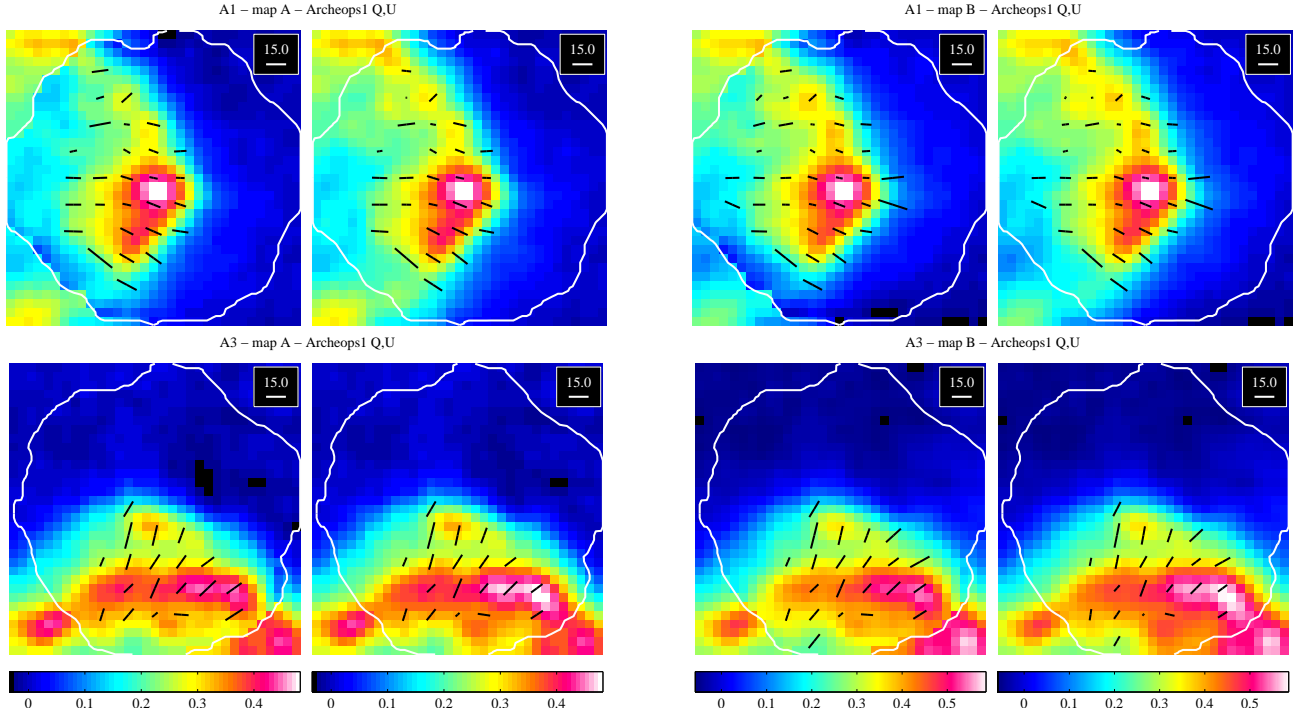


Figure 3. Simulated chopped and unchopped images as described in § 3.1. On the left of each sub-panel is the ‘chopped’ image, meant to represent the polarimetry data. Next to it on the right is the corrected image. The upper row is for region W and the lower row is region N. The scan-maps used are A and B and the Q and U model is *Archeops 1* (see Table 2 and § 3.1 for a detailed description). The effects of chopping on I can be mostly seen at the edges of the fields where the edge of the remnant was chopped onto (see Fig. 1).

Table 2. Results of simulated chopping onto polarised emission.

Model	Submm I map	p_{cor}	W: western field			N: northern field			
			p_{chop}	Δ_p	$\Delta\theta$	p_{cor}	p_{chop}	Δ_p	$\Delta\theta$
Scaled radio $Q, U \times 3$	A	11.1	11.9	+0.8	+0.4	13.0	13.7	+0.7	+0.9
	B	8.2	8.7	+0.4	+0.4	11.1	12.2	+1.0	+0.9
	C	10.6	11.1	+0.5	+0.4	See note*			
$Archeops\ 1$ $p = 23$ per cent, $\theta = -\pi/3$	A	10.7	11.9	+1.2	+1.2	12.5	13.7	+1.2	-0.7
	B	8.2	8.7	+0.5	+0.9	10.3	12.2	+1.9	-2.7
	C	10.4	11.1	+0.7	+0.5				
$Archeops\ 2$ $p = 12$ per cent, $\theta = \pi/8$	A	11.6	11.9	+0.3	-0.3	13.5	13.7	+0.2	+0.5
	B	8.5	8.7	+0.2	-0.3	11.7	12.2	+0.5	+1.6
	C	10.9	11.1	+0.2	-0.1				
Observed map	polarimetry		12.6 ± 1.2				15.1 ± 0.8		

Notes: Column (1) refers to the model used for Q and U in the reference positions; (2) submm scan-map used to determine the reference I value and combined with the measured submm Q and U to produce the quoted p values (see text); (3) mean p in the corrected map; (4) mean p in the ‘chopped’ map, error on the mean p is similar to that quoted for the polarimetry in the final row of the table (~ 1 per cent in each field); (5) $\Delta p = p_{chop} - p_{cor}$; (6) $\Delta\theta = \theta_{chop} - \theta_{cor}$. Columns 3–6 are repeated for positions W and N which each have different reference chop positions. * scan-map C cannot be used for position N as the background is too negative.

tion. In some specialised geometries, depolarisation can lead to an increase in fractional polarisation followed by a decrease at successively larger wavelengths, but this occurs only under conditions of very strong depolarisation (≥ 10 – Cioffi & Jones 1980), which does not apply in Cas A above 5 GHz. The lack of depolarisation at 5 GHz thus implies that the high 850- μ m polarisations arise from an independent source.

Another piece of evidence for internal depolarisation could have come from comparisons of depolarisation with X-ray bright-

ness, serving as a proxy for the density of the depolarising thermal electrons. Indeed, Anderson et al. (1995) showed a very strong correlation between the X-ray brightness and the depolarisation of emission between 5 GHz and 1.4 GHz, arguing for internal depolarisation at the low radio frequencies. However, no such dependence is seen in our comparison of depolarisation between 850 μ m and 5 GHz and the X-ray brightness (Fig. 5, left). Thus, the high fractional polarisations at 850 μ m must arise from another cause. This

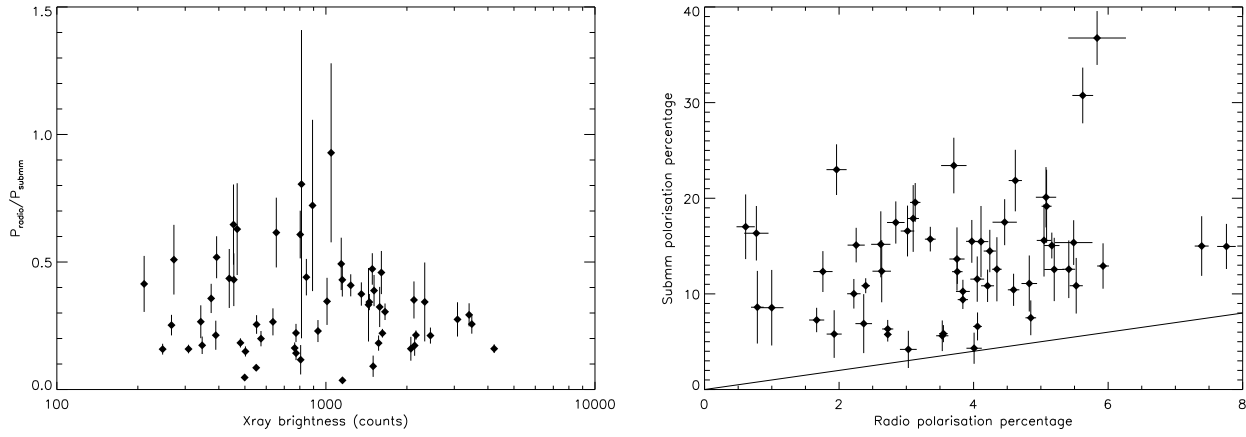


Figure 5. *Left:* Depolarisation from 5 GHz to 850 μm as a function of X-ray brightness. There is no clear relationship, unlike the 1.4-GHz to 5-GHz depolarisation which correlates strongly with X-ray brightness (Anderson et al. 1995). *Right:* Radio polarisation versus submm polarisation. The line shows a one-to-one correspondence. There is no obvious correlation.

850- μm -independence is also demonstrated in the plot of p_{radio} vs. p_{submm} in Fig. 5 (right) where no correlation is seen.

We now turn to the PA of the polarisation. In Fig. 6 we show the PAs (θ) of the radio and submm and 2.2- μm polarisation vectors (Jones et al. 2003) as a function of azimuth. The radio measurements have been corrected for the local Faraday rotation, re-determined from the data of Anderson et al. (1995). They quoted an average value of -110 rad m^{-2} , while we determine a range of values from -50 to -302 rad m^{-2} for our range of azimuths. The extrapolated rotations at 850 μm are <0.01 degrees, so no correction for Faraday rotation has been made for those, or for the 2.2- μm data.

There is a very good correlation between all three sets of measurements, suggesting that whatever is responsible for the extra polarisation signal in the submm waveband is related to the same magnetic fields that are responsible for the synchrotron emission at 5 GHz and 2.2 μm and, perforce, is intrinsic to Cas A and is not due to foreground material. The small mean offset between the corrected 5-GHz PAs and those at 850 μm and 2.2 μm are consistent with the systematic uncertainty in the RM correction. To first order the PAs all provide strong evidence for a radial magnetic field, as is common in young supernova remnants (Anderson et al. 1995).

If we take the submm and 2.2- μm magnetic field PAs at their face value, ignoring the systematic uncertainties, they agree very well with each other and are systematically offset from a radial angle by $\sim 10\text{--}20^\circ$ in a clockwise direction. At present, there is no apparent reason for this offset.

4 DISCUSSION

Since we cannot explain the submm polarisation as arising from synchrotron emission we will now consider the most likely alternative – that it is due to dust aligned with the magnetic field in the remnant. We will estimate p_d , the polarisation fraction of the dust in the remnant. We know that the submm flux we measure is a combination of radio synchrotron and thermal emission from dust, such that $I_s = I_r + I_d$. Similarly we can write that $Q_s = Q_r + Q_d$ and $U_s = U_r + U_d$. We can also express Q and U in terms of I , p and θ , as $Q = Ip \cos(2\theta)$ and $U = Ip \sin(2\theta)$. Combining these equations and solving for dust polarisation, p_d , gives:

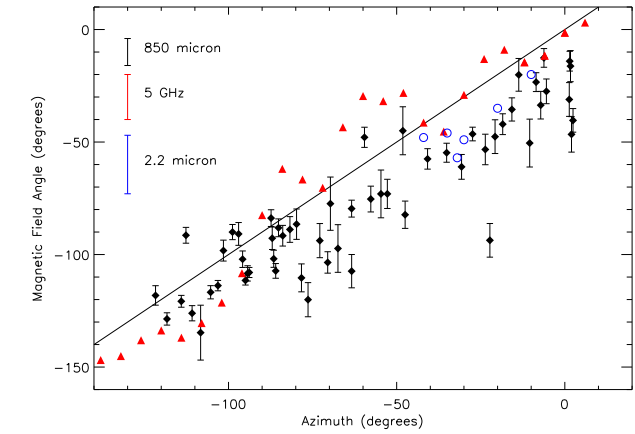


Figure 6. Inferred magnetic field angle ($\text{PA} - 90^\circ$) versus azimuth angle (0° for celestial north). Solid diamonds are 850- μm PAs; red triangles are 5-GHz PAs from Anderson et al. (1995) corrected for the local RM as described in the text; blue open circles are 2.2- μm PAs from Jones et al. (2003). Systematic errors bars are shown in the top left. The solid line shows a pure radial alignment.

$$p_d = \frac{[(I_s p_s - I_r p_r)^2 + 2 I_s p_s I_r p_r (1 - \cos 2(\theta_s - \theta_r))]^{1/2}}{I_d} \quad (5)$$

which for $\theta_s = \theta_r$ simplifies to

$$p_d = (p_s - p_r) \frac{I_r}{I_d} + p_s \quad (6)$$

The fractional dust polarisation calculated using Eqn. 6 is unprecedented, with an average $p_d = 30 \pm 2$ per cent. A histogram of p_d is shown in Fig. 7. Eqn. 6 assumes that the polarised synchrotron and dust radiation is emitted with the same intrinsic PA (i.e. aligns with the B field in the same way) and that any rotation between 5-GHz and 850- μm vectors is due to Faraday rotation at 5 GHz. This is a reasonable assumption given Fig. 6. We obtain a slightly higher value for p_d (33 per cent) if we use the difference between the RM corrected 5-GHz PA and the submm PA in Eqn. 5 instead.

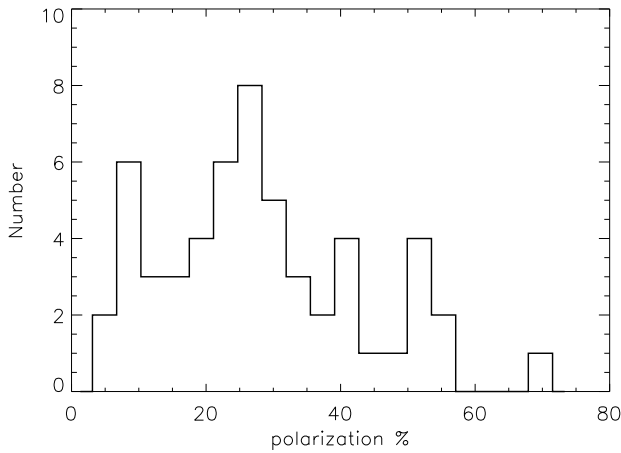


Figure 7. Histogram of dust polarisation fraction, p_d , calculated using Eqn. 6.

We can create a map of 850- μm dust flux density, I_d , by scaling the 5-GHz map to 850 μm as described in § 3.2. Subtracting the scaled synchrotron map from the 850- μm image leaves the 850- μm emission due to dust. This dust map⁴ is shown in Fig. 8, with the dust polarisation calculated from Eqn. 6. Over-plotted are CO(2–1) contours from Eales et al. (in preparation). This shows three things: first, there is dust emission in the northern part of the remnant, but no corresponding CO emission; second, the level of submm polarisation anti-correlates with the CO contours; the dust polarisation being lowest at the western peak, consistent with the suggestion by Krause et al. (2004) and Wilson & Batrla (2005) that its submm emission is contaminated by foreground clouds; third, there is polarised dust emission in both the north and the west.

The polarisation signal is correlated with the magnetic field in the remnant, which means that some of the emission in the western region must be associated with the remnant. None of dust intensity or polarised flux in the north is associated with molecular material. Thus the finding of Krause et al. (2004) that there is ‘no cold dust in Cas A’ is demonstrably incorrect. The average dust polarisation around the western peak is 13.7 ± 1.4 per cent; in the north, away from the CO, it is 39.4 ± 3.2 per cent. If we assume that the intrinsic value of p_d is similar throughout the remnant, we can use the uncontaminated values in the north to estimate the contribution of the foreground material to the western peak. Since $p \propto 1/I$, we simply correct the dust flux in the western peak by the ratio $13.7/39.4 = 0.34$, which gives a flux density of 0.83 Jy and a corresponding dust mass of $0.14 M_\odot$ for dust intrinsic to Cas A in the western peak (assuming $\kappa_{850} = 0.76 \text{ m}^2 \text{ kg}^{-1}$ and $T_d = 20 \text{ K}$; D03).

We can estimate a conservative minimum total dust flux density associated with the whole remnant by assuming that only the polarised flux density (~ 30 per cent) is intrinsic to the remnant. Using the integrated flux density from the dust map in Fig. 8, 20.1 Jy, we then have a total dust flux for Cas A at 850 μm of 6.0 Jy, based on our submm polarimetry. This produces a revised dust mass estimate, for $\kappa_{850} = 0.76 \text{ m}^2 \text{ kg}^{-1}$ and $T_d = 20 \text{ K}$, of $M_d \sim 1.0 M_\odot$. This value is consistent with theoretical predictions for

⁴ This map differs slightly from that in D03 as we have used a more accurate, spatially varying spectral index to extrapolate the radio synchrotron flux to the submm waveband.

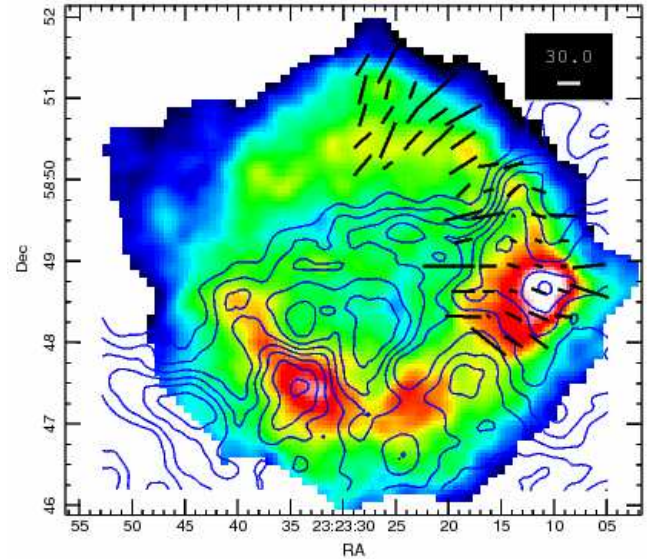


Figure 8. Synchrotron-subtracted 850- μm image, showing the location of the dust. Overlaid are the dust polarisation vectors calculated using Eqn. 6. Also shown in blue are CO(2–1) contours, at the same resolution (Eales et al. 2008, (in preparation)). CO contours coincide with the western dust peak, but the dust polarisation at these positions indicates that some of the 850- μm emission must be due to dust in the remnant. The decrease in dust polarisation at the CO peak in the west is consistent with some fraction of the submm emission at this location being due to foreground material, associated with the CO.

supernova dust yields (e.g. Todini & Ferrara 2001; Nozawa et al. 2003; Bianchi & Schneider 2007) and sufficient to explain the dust at high redshift (Morgan & Edmunds 2003; Dwek et al. 2007).

4.1 Grain alignment

What does this polarisation fraction tell us about the properties of the dust in Cas A? Average polarisation fractions in typical interstellar and molecular clouds are of the order 2–7 per cent (Hildebrand et al. 2000; Matthews & Wilson 2002; Curran & Chrysostomou 2007) though some clouds have values as high as 15–20 per cent (Benoît et al. 2004). We are unaware of any measurements as high as those quoted here, which suggests that either the dust or the alignment mechanisms in Cas A differ – perhaps unsurprisingly – from those in the general ISM.

Observations of polarised starlight and thermal emission from dust mean that there must be a population of dust grains which are non-spheroidal and a mechanism capable of aligning the grains so that an appreciable polarisation signal can be detected. The details of how interstellar dust aligns so efficiently, despite impacts by gas atoms acting to randomise their orientations, has kept theorists busy for half a century. The original proposal by Davis & Greenstein (1950, 1951) suggested paramagnetic alignment, where the axis of rotation of the slightly elongated grains becomes aligned with the B field though magnetic dissipation. This theory was unable to explain the polarisation levels observed in the ISM and star-forming regions because the timescales for alignment are longer than the timescales for randomisation by collisions with the gas.

There have been many significant improvements to the theory of grain alignment in recent years – see Lazarian (2007) for an excellent review. Several mechanisms are now thought to operate in different astrophysical environments. Briefly these

comprise radiative torques (Dolginov 1972; Draine & Weingartner 1996; Lazarian & Hoang 2007a; Hoang & Lazarian 2008a), mechanical alignment in a supersonic or subsonic gas flow (Gold 1952; Roberge et al. 1995; Lazarian 1997; Yan & Lazarian 2003; Lazarian & Hoang 2007b) and super-paramagnetic alignment (Lazarian & Hoang 2008).

The strong and turbulent magnetic field in Cas A ($B \sim 0.5$ mG – Wright et al. 1999), together with the large abundances of heavy elements and the presence of a hot X-ray plasma, means that certain mechanisms may be particularly applicable to the environment of Cas A. Pinwheel torques arising from the interaction of grains and electrons in a hot plasma (Hoang & Lazarian 2008b), supersonic mechanical alignment, sub-sonic mechanical alignment through MHD turbulence (Yan & Lazarian 2003) or grains with super-paramagnetic (e.g. Fe) inclusions (Lazarian & Hoang 2008) can all lead to highly efficient alignment. The timescales they have to operate is small in astrophysical terms, as the explosion of Cas A occurred only ~ 300 years ago. We note that the low synchrotron polarised fraction indicates a turbulent and disordered magnetic field on sub-arcsecond angular scales. This acts to reduce the observed polarisation as random orientations are averaged within the synthesised beam. If the dust grains were aligned with this tangled small-scale magnetic field then we might expect a similar beam depolarisation effect to operate at submm wavelengths. However, this would give rise to unphysical intrinsic dust polarisation fractions and so we believe that the alignment mechanism must be operating on larger scales. The radial B field in Cas A is ordered on large scales and thought to arise from Raleigh-Taylor instabilities at the reverse shock boundary (Gull 1975). These large-scale radial motions may also be responsible for aligning the dust in Cas A.

A full application of these models to Cas A is beyond the scope of this paper but these data should provide an interesting test of these theories and should shed light on the nature of the grains responsible for the polarised submm emission. Exotic grain shapes and compositions, such as the iron needles proposed by Dwek (2004), remain possible candidates to explain the submm emission from Cas A since they should produce a strong polarised signal and align rapidly. In such cases, the mass of dust could be substantially less than that estimated in § 4.

SUMMARY

- We have discovered unprecedented levels of submm polarisation towards the Cas A supernova remnant, significantly in excess of that expected from the radio synchrotron, and correlated with the magnetic field direction in Cas A.
- There is no currently known way to produce the polarised submm emission from a synchrotron process; a depolarising mechanism capable of producing a peak in f_{pol} as a function of wavelength would be required.
- The polarised emission is therefore strong evidence that some fraction of the cold dust detected by D03 is associated with the supernova remnant.
- The strength of the polarisation signal is unprecedented in the general ISM and indicates a highly efficient alignment mechanism at work in Cas A. These data provide a stringent test of grain alignment mechanisms, given the very short timescale available, ~ 300 yr.
- Alternatively, the strong signal may arise in exotic grains such as iron needles.
- Higher-resolution polarimetry at $850 \mu\text{m}$ is required to con-

firm the polarisation signal and provide a comparison at the spatial resolution of the radio synchrotron emission. Measurements of the high-frequency (100–200-GHz) synchrotron polarisation are required to test whether a perverse radio depolarisation mechanism is at work.

- Future far-IR and submm polarimeters, such as those planned for SCUBA-2 (Bastien et al. 2005) and *FIRI* (Helmich & Ivison 2008), will be able to image the submm polarisation in Cas A at higher resolutions and frequencies.

ACKNOWLEDGEMENTS

We wish to thank the JCMT staff that were involved in commissioning and maintaining the SCUBA Polarimeter. The data presented here were awarded under programme M04AU10. We also thank A. Chrysostomou, R. Curran, J. Greaves and G. Scheiven for helpful discussions on polarimetry data reduction, T. J. Jones for comments on the $2.2\text{-}\mu\text{m}$ data and acknowledge the input from undergraduate project student, S. Chowdhury.

REFERENCES

- Anderson M. C., Keohane J. W., Rudnick L., 1995, *ApJ*, 441, 300
 Bastien P., Bissonnette É., Ade P., Pisano G., Savini G., Jenness T., Johnstone D., Matthews B., 2005, *JRASC*, 99, 133
 Benoît A. et al., 2004, *A&A*, 424, 571
 Berry D. S., Gledhill T. M., 2001, *Starlink User Note* 223
 Bianchi S., Schneider R., 2007, *MNRAS*, 378, 973
 Blair W. P., Ghavamian P., Long K. S., Williams B. J., Borkowski K. J., Reynolds S. P., Sankrit R., 2007, *ApJ*, 662, 998
 Borkowski K. J. et al., 2006, *ApJ*, 642, L141
 Bowden M. et al., 2004, *MNRAS*, 349, 321
 Cioffi D. F., Jones T. W., 1980, *AJ*, 85, 368
 Curran R. L., Chrysostomou A., 2007, *MNRAS*, 382, 699
 Davis L. J., Greenstein J. L., 1950, *AJ*, 55, 71
 Davis L. J., Greenstein J. L., 1951, *ApJ*, 114, 206
 Dolginov A. Z., 1972, *Ap&SS*, 18, 337
 Douvion T., Lagage P. O., Cesarsky C. J., Dwek E., 2001, *A&A*, 373, 281
 Draine B. T., Weingartner J. C., 1996, *ApJ*, 470, 551
 Dunne L., Eales S., Ivison R., Morgan H., Edmunds M., 2003, *Nat*, 424, 285
 Dwek E., 2004, *ApJ*, 607, 848
 Dwek E., Galliano F., Jones A. P., 2007, *ApJ*, 662, 927
 Dwek E., Hauser M. G., Dinerstein H. L., Gillett F. C., Rice W. L., 1987, *ApJ*, 315, 571
 Eales S. A. et al., 2008, *MNRAS*, in preparation
 Gold T., 1952, *Nat*, 169, 322
 Greaves J. S. et al., 2003, *MNRAS*, 340, 353
 Gull S. F., 1975, *MNRAS*, 171, 263
 Helmich F. P., Ivison R. J., 2008, *Experimental Astronomy*, 15
 Hildebrand R. H., Davidson J. A., Dotson J. L., Dowell C. D., Novak G., Vaillancourt J. E., 2000, *PASP*, 112, 1215
 Hoang T., Lazarian A., 2008a, *MNRAS*, 388, 117
 Hoang T., Lazarian A., 2008b, *ArXiv e-prints*, 801
 Holland W. S. et al., 1999, *MNRAS*, 303, 659
 Jenness T., Lightfoot J. F., 1998, in *Astronomical Society of the Pacific Conference Series*, Vol. 145, Albrecht R., Hook R. N., Bushouse H. A., eds, *Astronomical Data Analysis Software and Systems VII*, p. 216

- Jones T. J., Rudnick L., DeLaney T., Bowden J., 2003, *ApJ*, 587, 227
- Kenney J. D., Dent W. A., 1985, *ApJ*, 298, 644
- Krause O., Birkmann S. M., Rieke G. H., Lemke D., Klaas U., Hines D. C., Gordon K. D., 2004, *Nat*, 432, 596
- Lagage P. O., Claret A., Ballet J., Boulanger F., Cesarsky C. J., Cesarsky D., Fransson C., Pollock A., 1996, *A&A*, 315, L273
- Lazarian A., 1997, *ApJ*, 483, 296
- Lazarian A., 2007, *Journal of Quantitative Spectroscopy and Radiative Transfer*, 106, 225
- Lazarian A., Hoang T., 2007a, *MNRAS*, 378, 910
- Lazarian A., Hoang T., 2007b, *ApJ*, 669, L77
- Lazarian A., Hoang T., 2008, *ApJ*, 676, L25
- Matthews B. C., McPhee C., Fissel L., Curran R., 2008, *ApJ*, submitted
- Matthews B. C., Wilson C. D., 2002, *ApJ*, 571, 356
- Matthews B. C., Wilson C. D., Fiege J. D., 2001, *ApJ*, 562, 400
- Meikle W. P. S. et al., 2007, *ApJ*, 665, 608
- Milne D. K., 1987, *Australian Journal of Physics*, 40, 771
- Morgan H. L., Edmunds M. G., 2003, *MNRAS*, 343, 427
- Murray A. G., Nartallo R., Haynes C. V., Gannaway F., Ade P. A. R., 1997, in *ESA Special Publication*, Vol. 401, Wilson A., ed, *The Far Infrared and Submillimetre Universe.*, p. 405
- Nozawa T., Kozasa T., Umeda H., Maeda K., Nomoto K., 2003, *ApJ*, 598, 785
- Priddey R. S., Isaak K. G., McMahon R. G., Robson E. I., Pearson C. P., 2003, *MNRAS*, 344, L74
- Priddey R. S., Ivison R. J., Isaak K. G., 2008, *MNRAS*, 383, 289
- Rho J. et al., 2008, *ApJ*, 673, 271
- Roberge W. G., Hanany S., Messinger D. W., 1995, *ApJ*, 453, 238
- Sparks W. B., Axon D. J., 1999, *PASP*, 111, 1298
- Sugerman B. E. K. et al., 2006, *Science*, 313, 196
- Todini P., Ferrara A., 2001, *MNRAS*, 325, 726
- Wang R. et al., 2007, *AJ*, 134, 617
- Wang R. et al., 2008, *ArXiv e-prints*, 806
- Williams R. M., Chu Y.-H., Gruendl R., 2006, *AJ*, 132, 1877
- Wilson T. L., Batrla W., 2005, *A&A*, 430, 561
- Wright M., Dickel J., Koralesky B., Rudnick L., 1999, *ApJ*, 518, 284
- Yan H., Lazarian A., 2003, *ApJ*, 592, L33

This paper has been typeset from a $\mathrm{T}_{\mathrm{E}}\mathrm{X}/\mathrm{L}^{\mathrm{A}}\mathrm{T}_{\mathrm{E}}\mathrm{X}$ file prepared by the author.